Research Paper

Verification of selective laser melting heat source models with *operando* X-ray diffraction data

Samy Hocine [a,b], Helena Van Swygenhoven [a,b,*], Steven Van Petegem [a]

[a] *Photons for Engineering and Manufacturing, Paul Scherrer Institut, Forschungsstrasse 111, 5232 Villigen PSI, Switzerland*
[b] *Neutrons and X-Rays for Mechanics of Materials, IMX, École Polytechnique Fédérale de Lausanne, Route Cantonale, 1015 Lausanne, Switzerland*

ABSTRACT

The output obtained from *operando* X-ray diffraction experiments on Ti-6Al-4V is used to verify the accuracy of four FEM models in predicting the temperature evolution of the solidified domain, the cooling rates of the α and β phases, and the influence of the scanning vector length on the duration of the β phase. Three different laser heat sources are considered: a simple ellipsoid, a double ellipsoid, and a cylindrical source with a parabolic penetration curve. The comparison between simulated and experimental results allows to verify the role of radiation loss and symmetric/asymmetric enhanced thermal conductivity on the cooling evolution. Furthermore, it is shown that the evolution of the lattice strains evidence the formation of residual stresses and can be used for the further development of phase field and thermomechanical inspired FEM-based models.

1. Introduction

Selective laser melting (SLM) has become popular in the metal industry, since it allows parts to be built net-shaped in a layer-by-layer fashion. Processing parameters such as laser power, scanning speed, hatch distance, layer thickness, and powder size distribution influence the final quality of the product. Varying the setting parameters changes the resulting microstructure [1–5]. Thus, the optimization procedure to find the best range of parameters to target a specific microstructure becomes tedious and repetitive.

Thus, there is a strong interest in using finite element method (FEM) based modelling to narrow down the material processing window, and thereby reduce the handling generated by testing numerous samples [6]. These models demand high computing power and, therefore, simulations are limited to single laser scan tracks, allowing to perform more iterations to refine the input parameters [7–10]. By refining the mesh size, it is possible to have a better spatial resolution on the complex heat gradients and capture the thermal shocks introduced by the laser, a necessary requirement to couple the laser scanning simulation with a thermo-mechanical model which aims at predicting residual stresses [11,12]. However, because of computational cost and speed, such small mesh sizes cannot be used to model larger scanning strategies or entire parts. To overcome this, a layer-by-layer approach can be adopted, by remeshing the layer being processed and introducing an average heat flux corresponding to the total power absorbed from the laser multiplied by the total scanning time of the layer [13]. Another approach is to use a dynamic remeshing, with a fine meshed volume which follows the laser heat source during scanning to ensure accurate information from this region of interest, leaving the rest of the model with a coarser mesh [14–18].

FEM models must go through a validation procedure to strengthen the confidence index of the generated computational outputs. Several methods are available to gather experimental data. A simple and popular method consists in post-mortem observation of the sample to extract the melt pool dimensions. By looking at the surface of the printed sample, information on the width of the melt pool can be obtained by measuring the width of the printed track [14,19]. The melt pool depth can be measured on a cross section perpendicular to the scanning vector direction [7–9,15,16,20]. For multi-phase material, it has been reported that it is sometimes possible to obtain information on the thermal history of the microstructure by studying the distribution of the different phases in the melt pool and heat affected zone [10]. Thermocouples connected to the building support have been used to record the temperature evolution in the sample during the printing process [21,22]. The resulting temperature curves can then be compared to the one extracted from the FEM simulation computed at the same location. Thermocouples have also been placed within the sample during the printing process [23]. However, this requires opening of the SLM

machine during the building process. Direct imaging of the melt pool with a high-speed camera provides a measure for the length of the melt pool [24,25]. Filtering the images and linking the emission spectrum of the molten phase to temperature values allows to map the actual temperature distribution at the surface of the melt pool with a resolution of 20 μm [26].

Operando SLM synchrotron X-ray diffraction experiments on a Ti-6Al-4V alloy [27,28] provided direct information on the local temperature evolution during laser scanning. Here, the temperature is derived from the shift of the position of the X-ray diffraction peaks with a time resolution of 50 μs. The experiments showed that the heat accumulation during processing depends on the scan vector length. When scanning a 2×2 mm^2 area using a 2 mm scanning vector length in a bi-directional fashion, as it is done, for instance, in island or chessboard scanning, the temperature in the sample remains high for an extended amount of time. Due to this heat accumulation, a large part of the scanned area remains into the high-temperature β phase while printing multiple tracks, and only transforms back to low-temperature α phase when the laser is sufficiently far away. In contrast, when scanning an 8×2 mm^2 area using an 8 mm scan vector length, the local temperature cycles between higher and lower regimes for each scanning line. Therefore, the material experiences a phase transformation between the α/α' and β phases. As demonstrated in [27], this difference in heat accumulation has an important effect on the prior-β grain size and the resulting α/α' lamellae after cooling down of the sample.

The aim of this paper is to use the data obtained from the *operando* experiments on Ti-6Al-4V to verify the accuracy of several FEM models and explore if models can capture the influence of the length of the scan vector. Four FEM models were considered: (1) the model of Zhang et al. [21], which was used in a phase field analysis to predict the resulting phases in Ti-6Al-4V based on the temperature evolution in the sample; (2) the model used by Mirkoohi et al. [8] to predict the melt pool shape; (3) the model used by Ali et al. [7], which introduces an enhanced thermal conductivity approach but neglects the radiation losses to predict the residual stresses in the sample; and (4) the same model of Ali et al. taking into account the heat losses by radiation. These four models were selected since they were recently used to simulate SLM processing of Ti-6Al-4V alloy.

2. Methods

2.1. FEM modelling methodology

2.1.1. Model geometry

Simulations were performed using the finite element analysis (FEA) software Abaqus/CAE [29]. Fig. 1a and b present the model geometries used to simulate the 8×2 mm^2 and 2×2mm^2 experimental samples, respectively. The simulated geometries are composed of a build plate with a coarse mesh and the printed sample with a finer mesh, as shown in Fig. 1c.

During *operando* experiments, a sample was printed with 5 layers, each of them being 30 μm thick, giving a total sample height of 150 μm. The sample in the simulation has dimensions of $8.4 \times 2.2 \times 0.15$ mm^3 for the 8×2 mm^2, and $2.4 \times 2.2 \times 0.15$ mm^3 for the 2×2 mm^2. It is divided into two subsections along the Z-direction: the first 30 μm correspond to a layer of freshly deposited powder with a $60 \times 60 \times 30$ μm^3 mesh size (orange); below, a 120 μm thick layer representing the already printed layers, simulated with a mesh size of $60 \times 60 \times 60$ μm^3 (blue). The mesh size of the sample part was selected to ensure convergence of the result within an acceptable computation time and be compatible with the laser spot diameter and hatch distance.

To reduce computation time, the size of the build plate that was simulated was restricted, the further environment was mimicked with boundary conditions. The build plate in the simulations has dimensions of $9.4 \times 2.7 \times 1$ mm^3 and $2.4 \times 2.7 \times 1$ mm^3 for the 8×2 mm^2 and 2×2 mm^2, respectively. The material properties of the build plate are
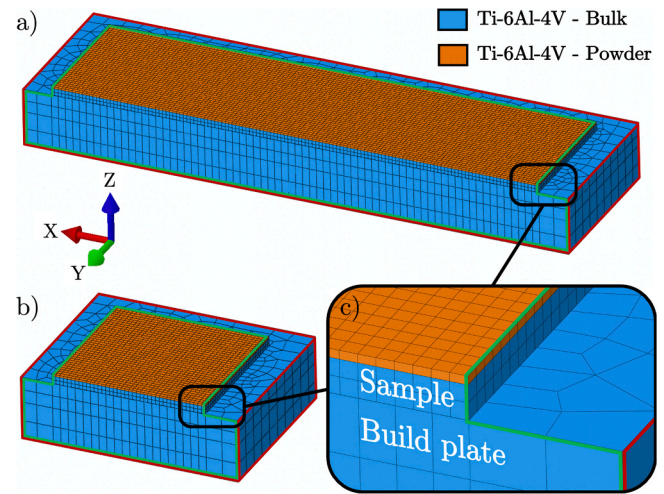

Fig. 1. (a) Simulation geometry for the 8×2 mm^2 sample and corresponding coordinate system; (b) Simulation geometry for the 2×2 mm^2 sample; (c) Zoom on the simulation geometry showing the sample and build plate. The surfaces highlighted in red correspond to a fixed-temperature boundary condition of 340 K, and the surfaces highlighted in green to the applied FILM condition to account for convection and radiation losses. (For interpretation of the references to colour in this figure legend, the reader is referred to the web version of this article.)

defined as bulk Ti-6Al-4V. The mesh size follows a gradient-like pattern with element dimensions going from 120 μm near the sample to 300 μm on the outer side. A DC3D8 (3D 8-node linear) element type was used to mesh all the parts. A fixed-temperature boundary condition of 340 K is applied on the bottom, back, and sides of the build plate section (Fig. 1, red). This temperature value was selected to agree with the temperature experimentally measured by a thermocouple on the substrate.

In Abaqus, the problem was modelled as an uncoupled heat transfer analysis in two stages. The first stage consists of a transient analysis of the laser scanning. An automatic time step increment was selected with a range between 10^{-8} s and 10^{-5} s, with an initial time step of 10^{-6} s. The total accumulated simulation time was 130.16 ms for the 2×2 mm^2 sample and 460.12 ms for the 8×2 mm^2 sample. The second stage consists of a transient analysis of the sample cooling, after the laser scanning is completed and the laser is switched off. Here, the automatic time step increment was selected within the range between 10^{-8} s and 10^{-4} s, with an initial time step of 10^{-6} s. These values were selected to allow convergence of the model. The total accumulated simulation time was 1 s for both samples. The equation solver was set to use a direct method, with a quasi-Newton solution technique. The extrapolation of the previous states at the start of each increment was set to use a parabolic function.

The laser scanning was modelled using the DFLUX subroutine, with a scanning direction along the X axis. In our previous work [27,28], we showed that a constant time offset was present between the temperature peaks during laser scanning which is the settling time of the scanning head, needed for the mirrors to change position from the end of one scanning track to the beginning of the following one. During this period, the laser is off. The experimentally measured settling time was 0.63 ms for bi-directional scanning and was considered in our laser scanning subroutine.

Heat losses were taken into account by applying a surface film condition to all exposed surfaces, i.e. the top and front of the sample and build plate assembly with the FILM subroutine (Fig. 1, green). Finally, the transformation from powder to bulk Ti-6Al-4V upon laser melting and solidification was implemented by using the USDFLD subroutine. More details are given in the following section.

2.1.2. Material properties

The thermophysical properties for the bulk Ti-6Al-4V are taken from Mills [30]. We consider here the density ρ, thermal conductivity k and the specific heat capacity C_p as presented in Fig. 2.

We consider the powder distribution as simple cubic, with a packing coefficient of 0.523 [31,32]. The powder density in Fig. 2 is obtained by multiplying the bulk density before the melting point by the packing coefficient. The thermal conductivity of the powder is obtained following the equation of Sih and Barlow [33]:

Table 1
Latent heat of Ti-6Al-4V [21,30].

Latent heat of fusion	2.86×10^5 J/kg		
Solidus	1877.15 K	Liquidus	1923.15 K
Latent heat of vaporization	9.83×10^6 J/kg		
Liquidus	3563.15 K	Vaporization	3663.15 K

$$\frac{k}{k_g} = \left(1 - \sqrt{1-\varphi}\right)\left(1 + \frac{\varphi k_R}{k_g}\right) + \sqrt{1-\varphi}\left\{(1-\phi)\left[\frac{2}{1 - \frac{Bk_g}{k_s}}\left(\frac{B}{\left(1 - \frac{Bk_g}{k_s}\right)^2}\left(1 - \frac{k_g}{k_s}\right)\ln\frac{k_s}{Bk_g} - \frac{B+1}{2} - \frac{B-1}{1 - \frac{Bk_g}{k_s}}\right) + \frac{k_R}{k_g}\right] + \frac{\phi k_{contact}}{k_g}\right\} \quad (1)$$

with k the thermal conductivity of the powder bed, k_g the thermal conductivity of the gas [34], k_s the thermal conductivity of the solid (Fig. 2), φ the porosity of the powder bed, k_R the thermal conductivity of the powder owing to radiation [33], ϕ the surface contact between particles (here we chose $\phi = 0.05$ [35]) and B the deformation parameter of the particles (we assume $B = 1$ for spherical particles). Since $\phi > 0.01$, we have $k_{contact} \approx k_s$. The values obtained after calculation (Fig. 2) are of the same order of magnitude as used in [36].

To simulate the transformation from powder to solid after laser melting, the USDFLD subroutine is used in Abaqus. The red curves for density (ρ) and thermal conductivity (k) in Fig. 2a and b describe the powder properties at the beginning of the simulation. When the temperature locally exceeds the melting point, the material transforms and follows the bulk properties describes by blue curves. The specific heat capacity (C_p) pictured in Fig. 2c is used for the bulk state or powder state. The latent heat of fusion and vaporization are given in Table 1.

2.1.3. Heat losses

The heat losses q_{loss} are modelled with the FILM subroutine in Abaqus through a film coefficient h [37] with:

$$q_{loss} = h \times (T - T_0) \quad (2)$$

with T the local surface temperature and T_0 is the sink temperature, both in Kelvin (room temperature, 298.15 K).

The idea is to establish a film coefficient that combines convection losses (h_c) and radiation losses (h_r). In the case of convection losses, the equation is:

$$q_{conv} = h_c \times (T - T_0) \quad (3)$$

The heat losses by convection are directly proportional to the value of h_c. In the case of radiation losses, the heat transfer is represented by the equation:

$$q_{rad} = \varepsilon\sigma\left(T^4 - T_0^4\right) \quad (4)$$

With ε the emissivity of the material and σ the Stefan-Boltzmann constant.

Eq. (4) can be rewritten:

$$q_{rad} = \varepsilon\sigma\left(T^2 + T_0^2\right)\left(T^2 - T_0^2\right) = \varepsilon\sigma\left(T^2 + T_0^2\right)(T + T_0)(T - T_0) \quad (5)$$

By introducing $h_r = \varepsilon\sigma\left(T^2 + T_0^2\right)(T + T_0)$ the radiation heat transfer coefficient, the Eq. (5) becomes:

$$q_{rad} = h_r \times (T - T_0) \quad (6)$$

Then by combining Eqs. (2), (3) and (6), one can write:

$$q_{loss} = q_{conv} + q_{rad} = h_c \times (T - T_0) + h_r \times (T - T_0) = (h_c + h_r) \times (T - T_0)$$
$$= h \times (T - T_0) \quad (7)$$

The film coefficient, which now combines convection and radiation losses, can be written as:

$$h = h_c + h_r = h_c + \varepsilon\sigma\left(T^2 + T_0^2\right)(T + T_0) \quad (8)$$

The emissivity of the material is temperature-dependent. The emissivity values were extracted from the measurements done by Yang et al. [10] and fitted as shown in Fig. 3. The equation obtained after fitting is:
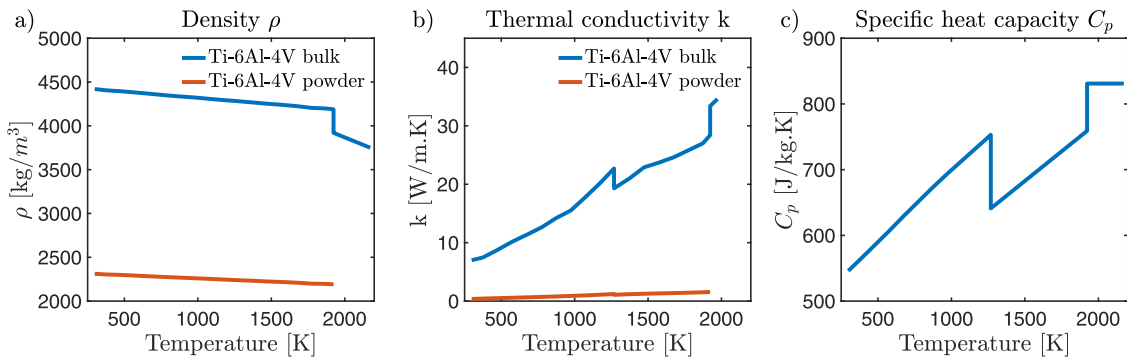

Fig. 2. Ti-6Al-4V thermophysical properties used in Abaqus; (a) Density of the bulk and powder; (b) Thermal conductivity of the bulk and powder; (c) Specific heat capacity of the bulk. The data for the bulk are taken from Mills [30].
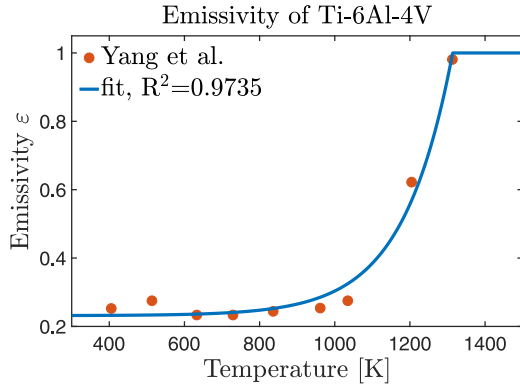
Emissivity of Ti-6Al-4V

Fig. 3. Emissivity curve for Ti-6Al-4V. The red markers are the experimental values taken from Yang et al. [10]. The blue curve is obtained after fitting the data, as shown in Eq. (9). (For interpretation of the references to colour in this figure legend, the reader is referred to the web version of this article.)

$$\varepsilon = \begin{cases} \varepsilon(T) & if \quad \varepsilon(T) < 1 \\ 1 & if \quad \varepsilon(T) > 1 \end{cases} \tag{9}$$

with $\varepsilon(T) = 0.231 + 3.06 \times 10^{-4} \exp\left[-7.55 \times 10^{-3}(4.19 \times (T - 273.15))\right]$.

2.1.4. Laser heat source models

Different laser heat source models were selected to compare the simulation outputs and experimental data obtained by X-ray diffraction. Table 2 gives an overview of the parameters of the different models. All the reported models are using volumetric heat sources, which is preferred compared to surface heat sources for the simulation of SLM processing [38].

2.1.4.1. Model 1: simple ellipsoid model (M1).
The first laser source model was taken from Zhang et al. [21] and consists of a volumetric Gaussian heat flux derived from the double ellipsoid model of Goldak [39]. The volumetric heat source equation is the following:

$$Q(x, y, z, t) = \frac{2\eta P}{abc\pi\sqrt{\pi}} \exp\left[-\left(\frac{(x + vt)^2}{a^2} + \frac{y^2}{b^2} + \frac{z^2}{c^2}\right)\right] \tag{10}$$

with η the absorptivity of the material, P the laser power, a, b and c the ellipsoid semi-axis, and v the scanning speed. Here $a = e.r$, $b = \frac{r}{e}$ and $c = d$ with e the melt pool eccentricity, r the laser radius, and d the penetration depth of the laser. In our simulation, we do not consider any eccentricity, so $e = 1$. The laser power was set at $P = 250W$ and the radius at $r = 50\mu m$. As reported by Zhang [21], the laser penetration was chosen to be within the powder layer, $d = 30\mu m$, and the laser absorption was set at $\eta = 55\%$.

In the model M1, Zhang at al. both radiation and convection losses are considered, with a heat transfer coefficient of 18 W/m² K [21] for

convection losses. We will consider a heat transfer coefficient $h_c = 20W/m^2.K$ to match the following models.

2.1.4.2. Model 2: double ellipsoid model (M2).
The second laser source is the one used by Mirkoohi et al. [8]. Four different heat source models are compared in the paper of Mirkoohi. The Gaussian semi-ellipsoid model from Goldak [39] was retained because it predicted the melt pool geometry over a wide range of process parameters. The heat source equation is the following:

$$Q(x,y,z,t) = \begin{cases} \dfrac{6\sqrt{3}f_f\eta P}{a_f bc\pi\sqrt{\pi}} \exp\left[-3\left(\dfrac{(x + vt)^2}{a_f^2} + \dfrac{y^2}{b^2} + \dfrac{z^2}{c^2}\right)\right] & for \quad x > vt \\ \dfrac{6\sqrt{3}f_r\eta P}{a_r bc\pi\sqrt{\pi}} \exp\left[-3\left(\dfrac{(x + vt)^2}{a_r^2} + \dfrac{y^2}{b^2} + \dfrac{z^2}{c^2}\right)\right] & for \quad x < vt \end{cases} \tag{11}$$

with η the absorptivity of the material, P the laser power; a_f, a_r, b and c the ellipsoid semi-axis, and v the scanning speed. Here a_f is the ellipsoid semi-axis in front of the laser, and a_r in the rear of the laser. Moreover, two additional coefficients – f_f and f_r – are introduced as the fraction of heat deposited in the front and rear of the heat source, where $f_f + f_r = 2$. For the sake of continuity on $x = 0$, we apply the constraint:

$$\frac{f_f}{a_f} = \frac{f_r}{a_r} \tag{12}$$

In the same fashion as the model of Zhang, the laser penetration was chosen to be within the powder layer, $d = 30\mu m$, and the laser absorption was set at $\eta = 55\%$. The laser power was set at $P = 250W$ and the radius at $r = 50\mu m$. We chose $a_f = r$ and $b = r$ and $c = d$. A 3-dimensional representation of the model is given in Fig. 4.

In the model M2, both radiation and convection losses are considered, with a heat transfer coefficient of $h_c = 20W/m^2.K$ for the convection losses [8].

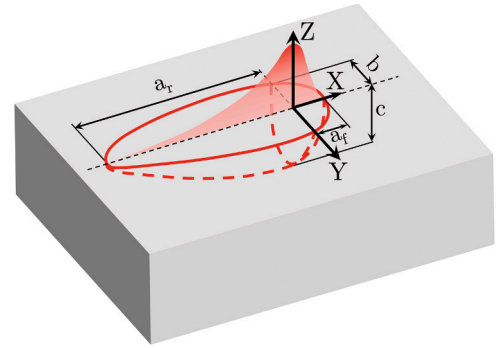**Fig. 4.** Graphic representation of Goldak's double ellipsoid model.

Table 2
Simulation summary.

Parameters	M1 (Zhang et al. [21])	M2 (Mirkoohi et al. [8])	M3 (Ali et al. [7])	M4 (Ali et al. [7])
Laser heat flux	Ellipsoid	Double ellipsoid	Cylindrical + Parabolic	Cylindrical + Parabolic
Absorption (η)	55%	55%	60%	60%
Convection losses (h_c)	20 W/m² K	20 W/m² K	20 W/m² K	20 W/m² K
Radiation losses (h_r)	Accounted	Accounted	Ignored	Accounted
Material properties	Mills [30]	Mills [30]	Mills [30] Enhanced k[7]	Mills [30] Enhanced k[7]

2.1.4.3. Models 3 and 4: cylindrical heat source with parabolic penetration depth (M3, M4). The third and fourth model are taken from Ali et al. [7]. The heat source expression is defined as a cylindrical heat source with a parabolic decay for the penetration in the material. The equation is the following:

$$Q(r,z) = I_r \times I_z \; with \begin{cases} I_r = 2.2032\eta\dfrac{P}{\pi r_0^2} & for \quad r < r_0 \\[2mm] I_z = -15z^2 + 4z + 2 & for \quad 0 > z > -250\,\mu m \end{cases}$$

(13)

With I_r the radial intensity of the laser, I_z the intensity penetration depth, η the absorptivity of the material, P the laser power and r_0 the laser spot radius. The laser power was set at $P = 250\,W$ and the radius at $r_0 = 50\,\mu m$, and the absorptivity was set at $\eta = 60\%$ as suggested by Ali.

Additionally, an enhanced thermal conductivity is considered to account for the Marangoni convection inside the melt pool [7]. The thermal conductivity for M3 and M4 is equal to:

$$k^*(T) = \lambda \times k(T) \; with \; \lambda = \begin{cases} 1 & if \quad T < T_{melt} \\ 4 & if \quad T > T_{melt} \end{cases}$$

14

With k the thermal conductivity in Fig. 2b, and λ the isotropic enhancement coefficient.

In the model M3, only the convection losses are considered, with a heat transfer coefficient of $h_c = 20\,W/m^2.K$; the radiation losses are ignored [7]. In the model M4, radiation losses are added to M3.

2.2. Experimental data used for validation

The temperature evolution during the printing of $8 \times 2\,mm^2$ and $2 \times 2\,mm^2$ Ti-6Al-4V samples *operando* during X-ray diffraction were used to compare with the FEM simulations. Details on the experiments can be found in [27,28].

Fig. 5 sketches a top view of the experimental setup showing the combination of laser scanning and X-ray beam on the sample. The substrate, a commercially available Ti-6Al-4V alloy, was covered with a 30 μm thick layer of Ti-6Al-4V ELI (extra low interstitial, grade 23) gas atomized powder (orange). The laser beam (red) was scanning with a hatch distance of 60 μm along the X-direction with a scanning vector length of 2 or 8 mm using a conventional bi-directional strategy over a 2 mm distance along the Y-direction. Up to 5 layers were printed. Details on the processing parameters are listed in Table 3.

The powder melts upon arrival of the laser and solidifies into a dense material (blue) when the laser has passed. A 12 keV gaussian X-ray beam is focused on the sample with an incidence angle of 15°, which results in an $80 \times 140\,\mu m^2$ (full-width at half-maximum – FWHM) elongated illuminated area (yellow), named A_X in the remaining of the paper. A 3D representation of the X-ray intensity distribution after projection on the sample is represented in Fig. 9, the red markers are the values used to calculate the temperature average in the simulation (detailed in Section 3). During the SLM process, X-ray diffraction patterns are collected by an EIGER detector [40] at a frequency of 20 kHz.

Ti-6Al-4V experiences a phase transformation upon heating and cooling. At room temperature, the alloy is in the α phase. Upon heating,
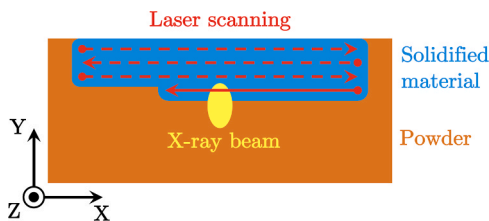
Table 3
Laser processing parameters.

Laser power	250 W
Laser spot size	0.1 mm
Laser wavelength	1070 nm
Scanning speed	600 mm/s
Hatch distance	0.06 mm
Layer thickness	0.03 mm

the $\alpha\rightarrow\beta$ phase transformation occurs at $T \approx 1270$ K, also called β transus, the latter being stable at high temperatures until the melting point. During cooling from the melt, first the high-temperature β phase appears which is stable until $T \approx 920$ K, followed by the low-temperature α phase. For cooling rates higher than 410 K/s, the martensitic α' phase appears [41]. Since the cooling rates obtained during SLM are above 10^3 K/s, a mixture of α/α' within the final microstructure is expected. Moreover, the initial microstructure of the powder is also α/α'. Both phases share the same hexagonal close-packed crystallographic configuration with close lattice spacing, which makes it difficult to differentiate them on X-ray diffraction patterns [42]. For that reason, the denomination "α/α' phase" will be used in this work.

Fig. 8a and b show the $\{01.2\}\alpha/\alpha'$ and $\{002\}\beta$ diffraction peaks during printing as intensity versus diffraction angle in time waterfall plots for the $2 \times 2\,mm^2$ and $8 \times 2\,mm^2$ samples, respectively. The peak positions 2θ, highlighted in purple and pink, are determined by their center of mass, the procedure is described in [28]. The relative change of the peak position allows calculating the elastic lattice strain ϵ of the crystal lattice as:

$$\epsilon = -\cot\left(\frac{2\theta}{2}\right)\frac{2\theta - 2\theta_0}{2}$$

(15)

with 2θ the center of mass of the peak and $2\theta_0$ the reference value here, taken at room temperature. Since the substrate is preheated to 340 K before printing (measured with a thermocouple), the initial peak positions are slightly shifted from their room temperature values due to thermal expansion. The value of $2\theta_0$ in Eq. (15) was derived using the thermal expansion of Ti-6Al-4V shown in Fig. 7 (detailed later in the text). The corresponding initial strain values at 340 K corresponds to $\epsilon(t = 0) = 4.9 \times 10^{-4}$.

Fig. 6a and b show the lattice strain evolution over time for the $\{01.0\}$, $\{00.2\}$, $\{01.1\}$ and $\{01.2\}$ α/α' reflections in the $2 \times 2\,mm^2$ and $8 \times 2\,mm^2$ samples respectively. Assuming the powder is strain-free, the increase in strain during heating reflects the thermal expansion, which is why the curves for the different reflections fall (mostly) on top of each other. During cooling after solidification of the β phase, residual stresses are expected to form due to the high heat gradients present in the material [43]. *Operando* experiments have shown that, until the $\beta\rightarrow\alpha/\alpha'$ phase transformation within the X-ray probed volume is completed, the β phase in the X-ray probed surface region experiences residual stresses while the laser scans neighboring lines [27]. In the $2 \times 2\,mm^2$ sample (Fig. 6a), the α/α' phase reappears at $t \approx 130$ ms and while cooling down (to approximately 340 K) the lattice strain decreases but with rates depending on the lattice reflection. By taking an average over the last 20 ms, the difference in lattice strain between the $\{01.0\}/\{00.2\}$ planes and the $\{01.1\}/\{01.2\}$ amounts 4×10^{-4}, suggesting the presence of residual strains. Fig. 6b shows a stronger divergence of the strain for the different reflections during cooling down of the $8 \times 2\,mm^2$. Even though the data is more scattered, the difference in lattice strain between $\{01.2\}$ and $\{01.0\}$ reaches 3.2×10^{-3}. Calculating residual stress from these results is beyond the scope of this paper. Besides elastic-plastic anisotropy of bulk Ti-6Al-4V, one needs also to take into account the difference in texture and α/α' needle morphology, as shown in [27].

Assuming that the lattice strain is mainly influenced by thermal effects, the average temperature T in the illuminated volume can be
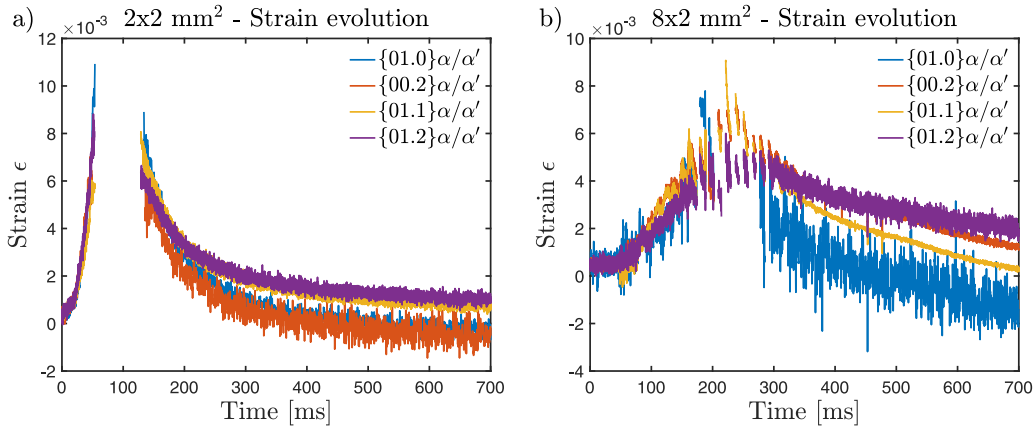

Fig. 5. Schematic of the experimental setup, the dashed lines represent the previous tracks scanned by the laser beam.

Fig. 6. Strain evolution of the α/α' phase in the 2×2 mm^2 (a) and 8×2 mm^2 (b) samples during laser scanning computed from Eq. (15) for different plane indices. The initial strain increase is attributed to the lattice expansion during heating, and the decrease to the lattice contraction during cooling. The gap in (a) comes from the fact that the α/α' phase is completely transformed into β at t $\approx$ 50 ms and transforms back at t $\approx$ 130 ms.
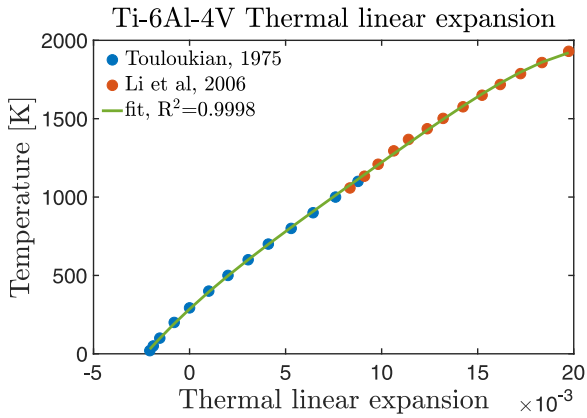

Fig. 7. Thermal linear expansion of Ti-6Al-4V as a function of the temperature with data from [44,45], fitted using a polynomial function.

determined by:

$$T = \frac{\epsilon}{\alpha_L(T)} \tag{16}$$

with $\alpha_L(T)$ the temperature-dependent linear thermal expansion coefficient.

For Ti-6Al-4V we did not find values for $\alpha_L(T)$ for the complete temperature range from room temperature up to the melting point obtained by one measurement technique. Therefore, we combine the values obtained from two references. Touloukian reports on $\alpha_L(T)$ for temperatures up to 1100 K based on the fitting on several datasets available in the literature [44]. Li et al. measured the volume expansion coefficient for Ti-6Al-4V around the melting point using electrostatic levitation measurements [45]. Assuming that Ti-6Al-4V behave isotropically, this change in volume can be linked to the linear thermal expansion:

$$\frac{\Delta V}{V} = 3\frac{\Delta L}{L} = 3\alpha_L \Delta T \tag{17}$$

Fig. 7 shows the resulting linear thermal expansion coefficient that was used to calculate the evolution of the temperature in the α/α' and β phases during printing, as shown in Fig. 8c–f.

Fig. 8c and d show the temperature evolution of the $\{01.2\}\alpha/\alpha'$ (purple) and 002β (pink) phase derived from the diffraction data using Eq. (16) for the 2×2 mm^2 and 8×2 mm^2 sample, respectively. Fig. 8e and f show a zoom in on the temperature profiles around the cycle for

which the laser and the X-ray probed volume coincide. In the 2×2 mm^2 sample this is around 65 ms and in the 8×2 mm^2 sample this is at 230 ms. As discussed in [27], the results clearly show that during laser scanning the X-ray probed surface region remains in the β phase in the small sample, whereas in the 8×2 mm^2 sample the material is experiencing cycles between α/α' and β.

Because the α/α' diffraction pattern is an overlap of two different series of peaks coming from the α and α' phases [42], a slight peak doubling is observed in some of the reflections we measured. The $\{01.2\}\alpha/\alpha'$ reflection was chosen since it does not show any strong peak doubling, which could influence the calculation of the temperature. The $\{002\}\beta$ reflection was selected as the only stand-alone β peak on the diffraction pattern.

The flat part of the temperature profile derived from the β peak position is evidence of the melt pool crossing A$_X$. The explanation of this curve shape is discussed in Section 4.2. This is in particular visible in Fig. 8e for the 2×2 mm^2 sample at t $\approx$ 65 ms, but also in Fig. 8f for the 8×2 mm^2 sample at t $\approx$ 230 ms. This plateau lasts 0.9 ms in both the 2×2 mm^2 and 8×2 mm^2 samples and can be correlated with a length of the melt pool of 540 μm passing A$_X$ at a scanning speed of 600 mm/s.

3. Results FEM simulations

The temperature profiles were extracted by taking a weighted average of the nodal temperature of 42 nodes at the center of the sample, where the X-ray beam is positioned (Fig. 5). These nodes represent a volume corresponding to the probed X-ray volume with an area of 120×360 μm^2 and a depth of 30 μm, the mesh height of the powder layer (accounting for the X-ray penetration in the material). They are separated into two groups of 21 nodes positioned on top of each other. In the (X,Y) plane the spacing among the nodes is 60 μm. In the Z-direction, they are separated by 30 μm. To calculate the average nodal temperature in the simulations, the nodes positioned on top of each other (Z-direction) are first averaged. A weighting function corresponding to the X-ray beam intensity distribution is then applied to the remaining 21 nodes. Fig. 9a shows the resulting group of 21 nodes superimposed to the multivariate Gaussian intensity distribution, Fig. 9b shows a top view in the (X,Y) plane.

Since the experimental temperature profile does not include the temperature of the molten phase, only the nodes that have a temperature below 1913.15 K, for which the material is solid, are considered for the weighted averaging. The resulting temperature follows the equation:

$$\overline{T} = \sum_i \frac{m_i T_i}{m_i} \text{ with } m_i = \begin{cases} m_i & \text{if } \quad T_i < T_{melt} \\ 0 & \text{if } \quad T_i > T_{melt} \end{cases} \tag{18}$$
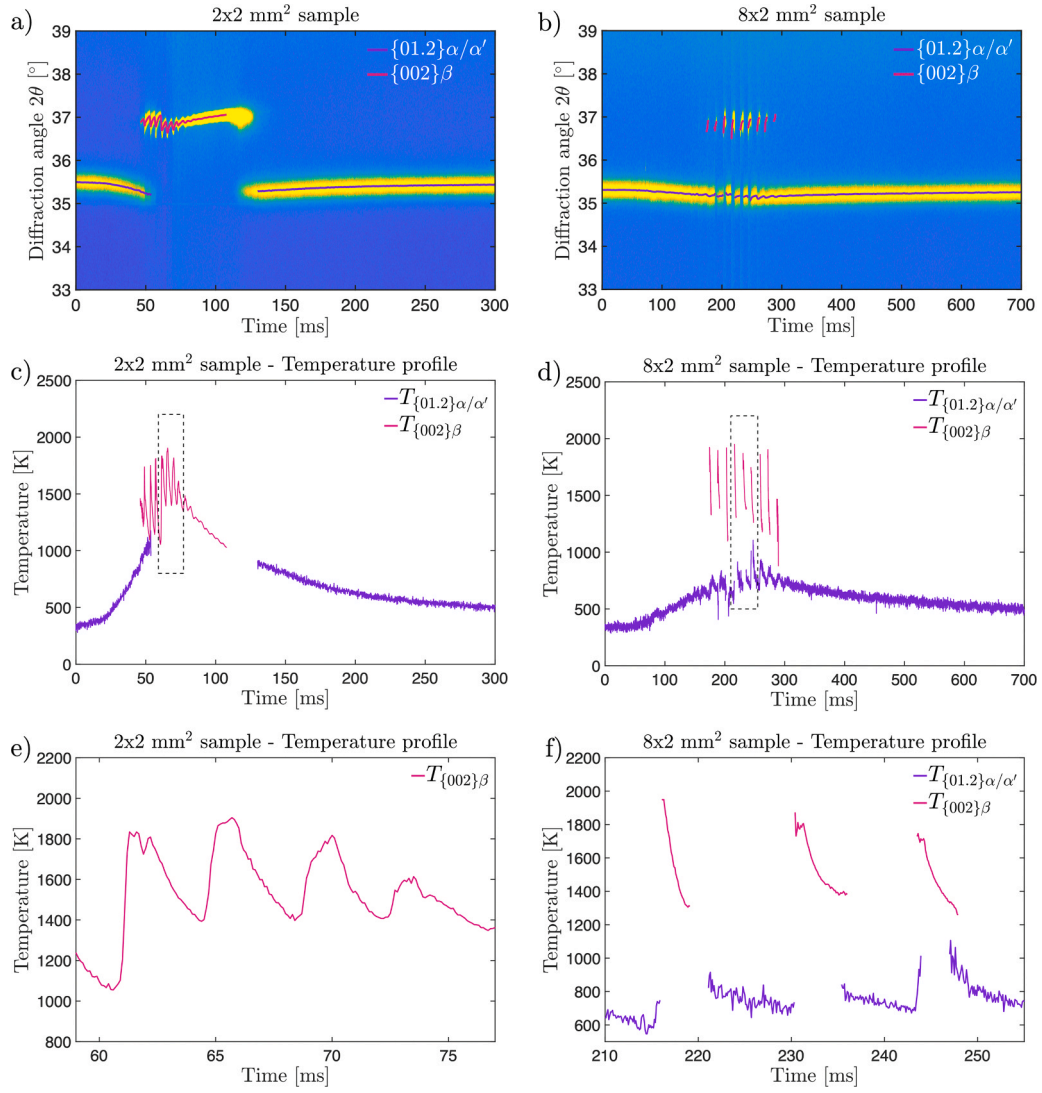
Fig. 8. (a,b) X-ray diffraction pattern with center of mass highlighted for the 2×2 mm^2 and 8×2 mm^2 samples; (c,d) Extracted temperature profile from the peak position in (a) and (b); (e,f) Zoom on the dashed area in (c) and (d). In the gap in (c) between 120 ms and 130 ms, the β and α/α' peaks co-exist in the probed volume, and peak position is influence by both temperature and lattice strain [28].
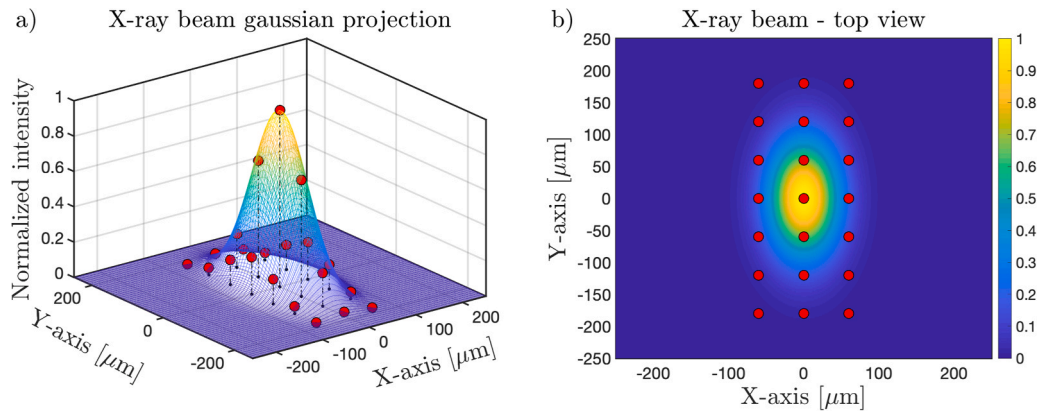

Fig. 9. (a) 3-dimensional representation of the X-ray gaussian intensity distribution with an 80×140 μm^2 FWHM. The red markers present the position of the nodes used to calculate the average temperature in the simulation. The vertical dashed lines represent the projection of the markers onto the (X,Y) plane. (b) Top view of the X-ray gaussian intensity distribution (to be compared with Fig. 5).
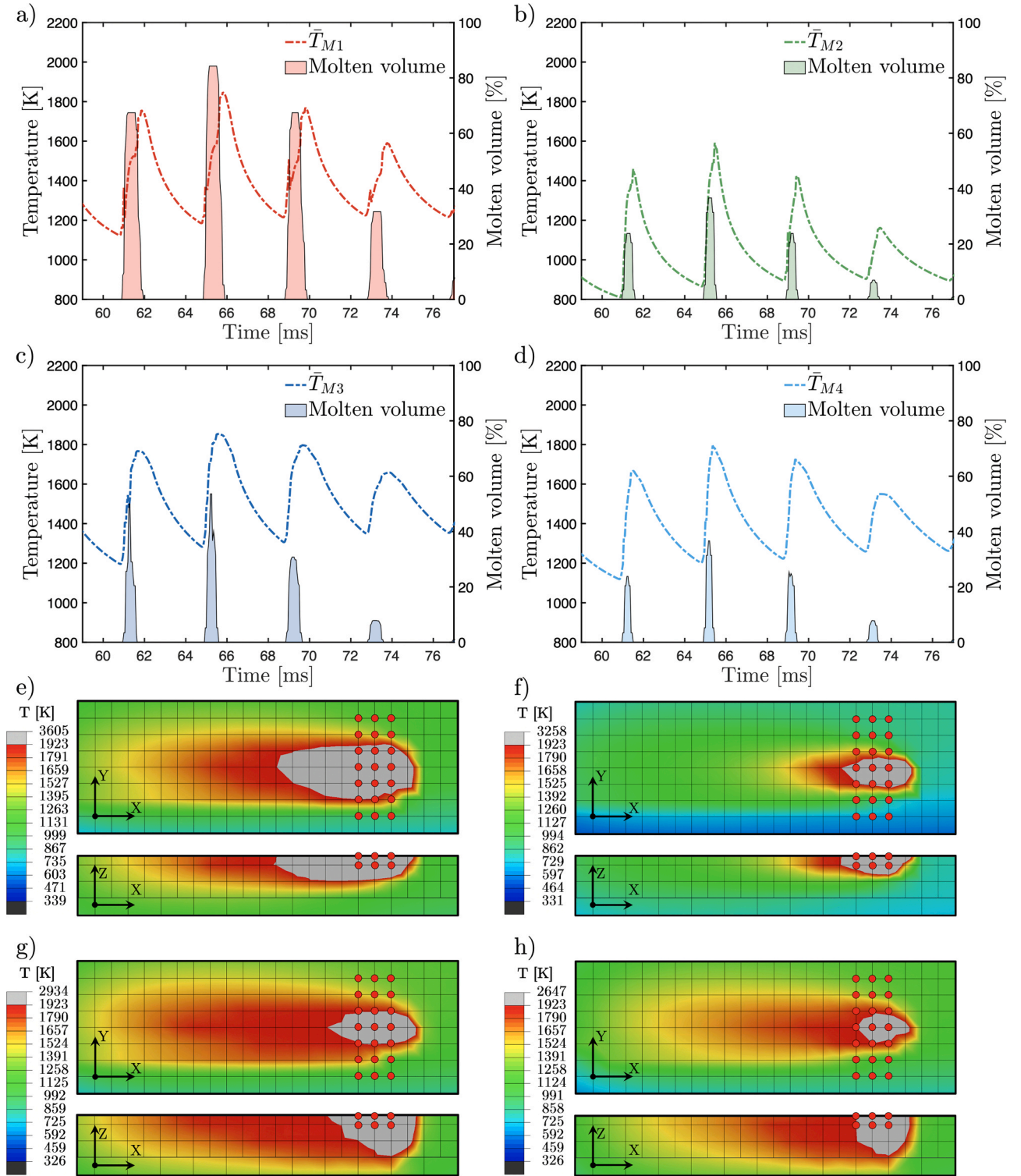
Fig. 10. Average temperature and molten volume interaction with A_X for: (a) M1; (b) M2; (c) M3 and (d) M4. (e)–(h) Top view and cross-section of the simulated melt pools for models M1 to M4 at t ≈ 65 ms, when the laser beam overlaps with A_X.

With $\overline{T}$ the weighted average temperature, T_i the nodal temperature, m_i the weighting coefficient from the X-ray intensity profile (Fig. 9) and T_{melt} the melting point of Ti-6Al-4V.

3.1. 2 × 2 mm² sample

Fig. 10a–d provides for the 4 models the simulated temperature

evolution (dashed) and the evolution of the molten volume percentage (filled curve) as a function of time for the cycles close to the time when the laser crosses the probed volume A_X. Because only the nodes outside of the molten volume are used to calculate the weighted average, as shown in Eq. (18), the size of the molten volume influences the shape of the temperature evolution. This causes a change in slope during heating, as is visible for model M1 (Fig. 10a) which has the highest molten volume percentage. Fig. 10e-f show the melt pool dimensions at t ≈ 65 ms
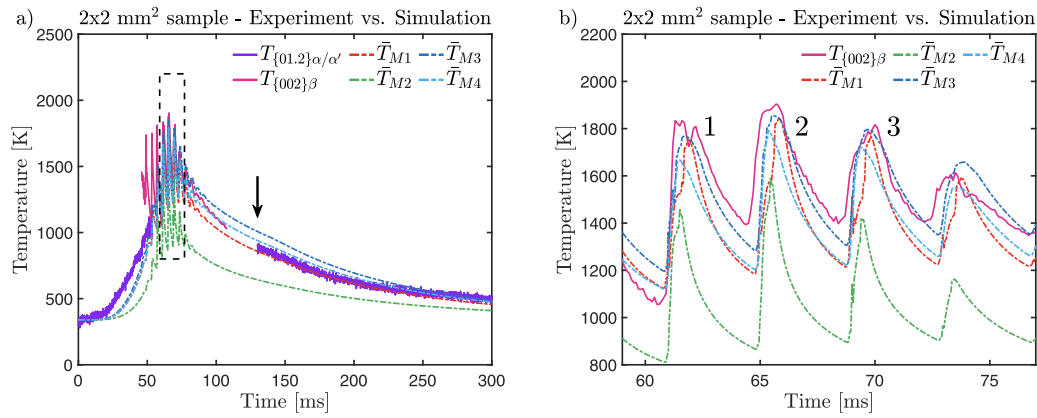
Fig. 11. (a) Experimental temperature profile presented in Fig. 8c together with the temperature profile of the $\{01.2\}\alpha/\alpha'$ and $\{002\}\beta$ reflections in purple and pink, respectively, with superimposed the simulated results for models M1 to M4 in dashed lines. The black arrow indicates the end of the laser scanning.; (b) Zoom on the highlighted area in (a). (For interpretation of the references to colour in this figure legend, the reader is referred to the web version of this article.)

for the four models with a view from the top and the middle cross-section along the X-axis. The black lines show the mesh size (60 μm in X-Y plane, 60/30 μm in Z-direction for solid/powder respectively). The red dots show the position of the nodes used for the calculation of the average temperature.

Fig. 11a compares the simulated temperature profile for the four models (dashed lines) with the experimental results for the $\{01.2\}\alpha/\alpha'$ and the $\{002\}\beta$ reflections. The laser scanning starts at t = 0 ms and finishes at t ≈ 130 ms, which is indicated by the black arrow. The experimental temperature evolution in the probed volume exhibits three regimes: (1) heating-up of the α/α' phase until the first signal from the β phase is observed at t ≈ 48 ms; (2) cycling within the β phase while the laser is scanning, the highest temperature is reached when the laser overlaps with A_X at t ≈ 65 ms; (3) cooling down after the laser is sufficiently far away from A_X, i.e. from t ≥ 76 ms on, during which the β phase disappears and the α/α' phase is formed. All 3 regimes are also observed in the simulated curves (without phase information). All models have difficulties in predicting the temperatures measured during heating-up in the first regime. Fig. 11b zooms into the second regime around the cycle for which the maximum temperature is obtained, corresponding to the time when the laser spots overlaps with A_X (t ≈ 65 ms).

The model M1 (Fig. 11a and b, red) seems to predict quite well many aspects of the experimental temperature profile of the laser scanning for the 2 × 2 mm² sample. When the laser and X-ray coincidence is maximal, the simulated profile tends to underestimate only slightly the experimental data (Fig. 11b). The temperature rise in this cycle is a bit delayed which can be attributed to the larger width of the melt pool (Fig. 10e), leaving fewer remaining nodes for the calculation of the average nodal temperature. After completing a 2 × 2 mm² layer, the cooling down matches the experimental curve well.

The model M2 (Fig. 11a and b, green) underestimates the temperature profile of the β phase during the coincidence cycle (t ≈ 65 ms) by 400 K on average. Furthermore, the overall heating and cooling curves of the α/α' phase (Fig. 11a) are lower compared to the other models. The melt pool size (Fig. 10f) is rather small, it has a length of approximately 250 μm (X-direction), a width of around 100 μm (Y-direction), and a depth of around 70 μm (Z-direction).

The model M3 (dark blue) matches well the temperature curve in the high-temperature β regime (Fig. 11b). It also predicts much better the initial heating-up during the deposition of the first lines (Fig. 11a). In the cooling part of the temperature curve (Fig. 11a, after t ≈ 80 ms), the model tends to overestimate the experimental α/α' temperature by almost 200 K, which can be ascribed to the fact that radiation losses are not included [7]. The melt pool (Fig. 10g) has an interesting profile, it goes quite deep compared to the models M1 and M2. It has a length of

around 330 μm (X-direction), a width of around 120 μm (Y-direction) and a depth of around 150 μm (Z-direction). This very deep melt pool is likely due to a combination of the enhanced thermal conductivity and the parabolic penetration depth. The heat penetration goes down to 250 μm compared to a penetration depth restricted to the first layer in the case of M1 and M2. This results in a consequently larger heated volume, as seen by the spread of the red area in the tail of the melt pool (Fig. 11e).

The model M4 (cyan), which adds radiation loss to M3, reduces the maximal temperature that is reached and brings down the temperature profile in the high-temperature β regime (Fig. 11b) as well as during the cooling after printing the complete layer. The heating part of the temperature when the laser approaches A_X remains the same. By comparing Fig. 10g and h, one can see that the width and depth of the melt pool are comparable between M3 and M4. In M4, a width of 110 μm is obtained in the Y-direction and a depth of 140 μm in the Z-direction. In other words, adding radiation loss reduces the length of the melt pool to 130 μm.

3.2. 8 × 2 mm² sample

The 8 × 2 mm² model contains around 4 times more elements than the 2 × 2 mm² model, so the computation time is much longer. For that reason, we chose to simulate the 8 × 2 mm² sample for only the models M1 and M4.

Fig. 12a and b show the comparison between the simulated (dashed lines) and experimental temperature evolutions obtained from the X-ray data (Fig. 8d). The laser scanning starts at t = 0 ms and finishes at t ≈ 460 ms which is indicated by the black arrow. Fig. 12b zooms in around t ≈ 232 ms, the time when the laser spot overlaps with A_X. Fig. 12c and d show the melt pool dimensions at t ≈ 232 ms for the two models M1 and M4 with a view from the top and a middle cross-section along the X-axis.

Due to the larger scan vector used in the 8 × 2 mm² sample, the phase transformation from α/α' to β occurs during each line scan. The simulated temperature is averaged over the nodes and provides no phase-specific information. Similar as for the 2 × 2 mm² sample, three regimes can be recognized in the temperature evolution: (1) heating during the first line scans, the X-ray probed volume remaining in the α/α' phase (Fig. 12a, until t ≈ 180 ms); (2) cycles close to the scan line overlapping with A_X (here the experimental curve shows the β and α/α' phases) including the line with the maximum temperature (Fig. 12b, at t ≈ 230 ms); and (3) cooling after the last signal coming from the β-phase has disappeared (Fig. 12a, from t ≈ 290 ms).

The simulated melt pool dimensions are smaller in the 8 × 2 mm² sample when compared with the 2 × 2 mm² sample. This can be
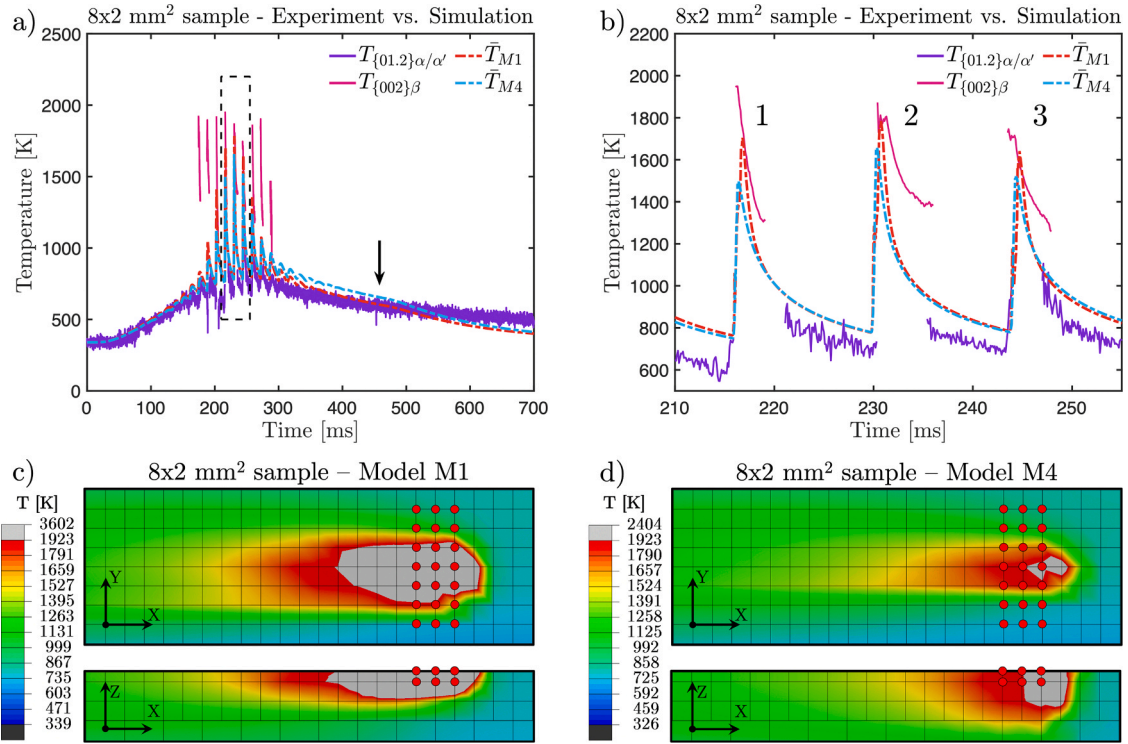
Fig. 12. (a) Experimental temperature profile presented in Fig. 8d with the temperature profile of the $(01.2)\alpha/\alpha'$ and $\{002\}\beta$ reflections in purple and pink, respectively, with simulated results for models M1 and M4 superimposed in dashed lines; (b) Zoom on the highlighted area in (a); (c) and (d) Top view and cross-section of the simulated melt pools for models M1 and M4 at $t \approx 232$ ms, when the laser beam overlaps with A_X. (For interpretation of the references to colour in this figure legend, the reader is referred to the web version of this article.)

explained by the larger scanning vector, reducing overall heat accumulation in A_X, and the larger sample representing a stronger heat sink. As a result, the thermal gradient around the melt pool is higher and the melt pool becomes smaller. The melt pool of M1 (Fig. 12c) has an elongated profile along the X-direction with a length of 450 μm. It is still shallow in the Z-direction, with a depth of 80 μm. The width is similar to the 2×2 mm^2 sample with 200 μm along the Y-direction. For the model M4 (Fig. 12d), the obtained melt pool is very small, it has a length of 140 μm along the X-direction, a width of 70 μm along the Y-direction, and a depth of 110 μm in the Z-direction.

During laser scanning of the first lines, before A_X is reached, the two models predict well the increase in temperature of the α/α' phase. (Fig. 12a). The predicted temperatures of the β phase at $t \approx 230$ ms, when the laser coincides with A_X, are close to the experimental one. The predicted cooling curve does however not follow the experimental cooling from the β and the α/α' phase. Here, one has however to take into account that the transformation is not homogeneous over the experimentally probed volume and that the temperatures are derived from the individual diffraction peaks, whereas the simulation does not provide information on phase composition. During cooling of the α/α' phase ($t > 290$ ms), M4 predicts slightly higher temperatures than experimentally measured. At $t \approx 460$ ms, when the laser is switched off, the simulated curves show a small change in the slope and the X-ray probed volume starts cooling faster.

3.3. Melt pool depth and width and optical microscope images of cross section

The experimental melt pool dimensions are determined from single line prints [46]. A total of 12 single tracks were printed on a Ti-6Al-4V substrate after the deposition of a 30 μm thick powder layer using the same printing parameters (Table 3). Fig. 13 shows the cross-section of a track after printing after mechanical polishing and etching with Kroll's
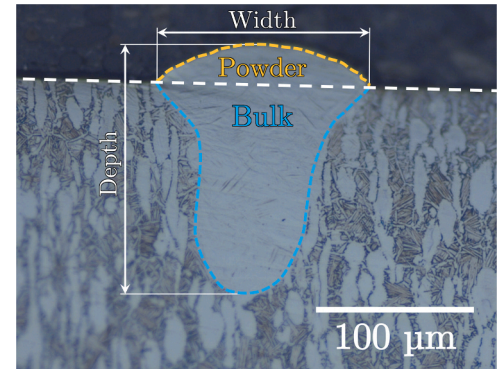

Fig. 13. Cross-section of a single track. The contrast between the light α/α' phase of the weld bead and the darker $\alpha + \beta$ microstructure allows to distinguish clearly the size of the melt pool. The part corresponding to the fused powder is highlighted in orange, and the melted substrate in blue. The measurements of the width and depth of the melt pool are also indicated by the arrows. (For interpretation of the references to colour in this figure legend, the reader is referred to the web version of this article.)

Table 4

Average width, depth and standard deviation obtained after melt pool measurements

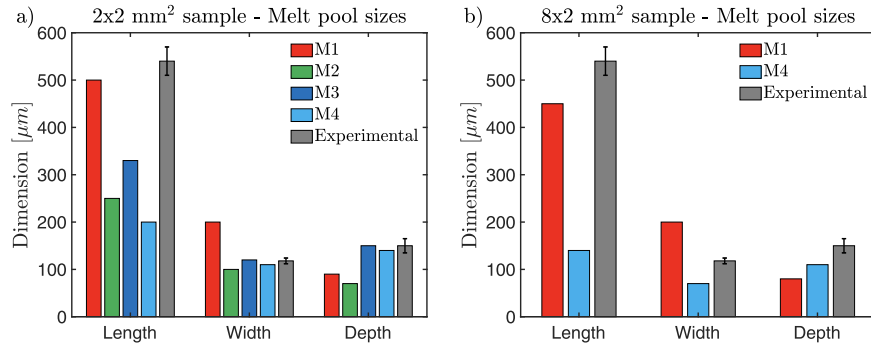|	Mean	Standard deviation
Width [μm]	118	6
Depth [μm]	150	15
Aspect ratio	1.28	0.17

Fig. 14. Melt pool sizes comparison for the 2×2 mm^2 sample (a) and the 8×2 mm^2 sample (b) with the experimental results.

reagent. The α/α' microstructure of the melt pool appears in light grey, surrounded by the $\alpha + \beta$ microstructure of the Ti-6Al-4V substrate [46].

The average measured width and depth and their standard deviation are respectively 118 ± 6 μm and 150 ± 15 μm, as listed in Table 4.

4. Discussion

4.1. Melt pool dimensions

The melt pool dimensions obtained in the simulations are summarized in Fig. 14 for the 2×2 mm^2 (a) and the 8×2 mm^2 sample (b). The experimental values including the standard deviation are also provided. The melt pool width and depth are taken from Table 4. To obtain the experimental value of the length of the melt pool, the flat part of the temperature profile derived from the X-ray data in Fig. 8e and f are used. The error bar is derived from the detector time resolution, ± 50 μs, resulting in an uncertainty of ± 30 μm on the melt pool length.

The melt pool dimensions obtained for the simulated results are taken from Fig. 10e–h for the 2×2 mm^2 sample, and Fig. 12c and d for the 8×2 mm^2 sample. The width and length are measured in the top view, and the depth is measured in the cross-section view."

According to the results for the 2×2 mm^2 sample, M1 predicts the length of the melt pool at best. However, the model overestimates the width and depth of the melt pool. Model M2 tends to underestimate all three dimensions. Models M3 and M4 are underestimating the length but are quite accurate regarding the width and depth.

The difference between M1 and M2 can be explained by the steeper gradient in the laser energy distribution of M2.

By looking at Eq. (10), the exponential decay constant is equal to -1 at $r = r_0$. Which means:

$$Q(r_0) = \frac{1}{e} \times Q(0) \approx 0.37 \times Q(0) \qquad (19)$$

with $Q(r_0)$ the heat flux at the laser radius and $Q(0)$ the heat flux at the center of the laser beam. In other words, the heat flux at the laser radius is still 37% of the heat flux at the center of the laser beam, explaining the large spread of the melt pool. The volumetric heat source Eq. (11) for M2 has an exponential decay constant equal to -3 at $r = r_0$. Which means:

$$Q(r_0) = \frac{1}{e^3} \times Q(0) \approx 0.05 \times Q(0) \qquad (20)$$

The heat flux at the laser radius is only 5% of the heat flux at the center of the laser beam and the energy distribution is, therefore, more concentrated around the center of the laser beam, resulting in smaller melt pool dimensions.

The introduction of deeper heat penetration in model M3 and M4 provides good predictions for the depth of the melt pool. The enhanced isotropic thermal conductivity is probably responsible for the better prediction of the width, it can however not predict the melt pool length accurately. Note that taking into account the radiation losses in M4

increases the underestimation of the melt pool length. However, it has little influence on the predicted width and depth.

The influence of the scan vector on the simulation predictions seems to be more important in M4 than in M1. The predicted melt pool length in M1 is 10% less in the 8×2 sample compared to the 2×2 sample, but the width and the depth are hardly affected. For the model M4, all the dimensions are considerably more reduced when a larger scanning vector is used: 30% for the melt pool length, 36% for the width, and 21% for the depth.

It is important to remember that the experimental values for the width and depth of the melt pool are derived from a single line scan (see Section 3.3). During the printing of a single track, the surrounding material is cold, which results in a high thermal gradient between the melt pool and substrate. On the contrary, during multiple track scanning, heat is accumulated in the sample, which results in lower thermal gradients. The higher thermal gradient between the melt pool and the surrounding material in a single track means that there is more heat extracted from the melt, and therefore the melt pool is cooling down faster. As a result, the size of the melt pool for the single-track scanning is expected to be smaller than for a multiple track scanning.

Moreover, during multiple track scanning, the local heat accumulation is higher when the scan vector length is shorter. Therefore, the thermal gradient is higher in the case of the 8×2 mm^2 sample, as confirmed in the temperature curve and melt pool images (Fig. 12). For that reason, the experimental melt pool dimensions in the 2×2 mm^2 samples might be slightly larger than in the 8×2 mm^2 sample for the same printing parameters. Nevertheless, this conclusion does not change the fact that the simulated results of the melt pool dimensions are underestimating the experimental results in general.

4.2. Temperature evolution in the X-ray probed volume

4.2.1. When the laser approaches

Fig. 15 zooms on the temperature evolution in the X-ray probed surface region before the local temperature is high enough to reach the β transus: (a) in the 2×2 mm^2 and (b) in the 8×2 mm^2 sample. The experimental temperature rises linearly between 400 and 850 K in both samples: the rate amounts -1.7×10^4 K/s in the small sample and -2.5×10^3 K/s in the large sample. In the large sample, the temperatures predicted by M1 and M4 are in good agreement with the experiment. In the small samples, the predicted temperatures are lagging for all models. Around 440 K, the heating rates are comparable with the experimental one, their values are shown in the caption of Fig. 15a. When the laser approaches further A_X and the temperature rises, the heating rates are increasing and the simulated temperature catches up with the experimental one.

4.2.2. Cooling rates during laser scanning across A_X

Fig. 16a and b show for the 8×2 mm^2 sample, a zoom around the $\{002\}\beta$ peak of the diffraction pattern during cycles 1 and 2 shown in
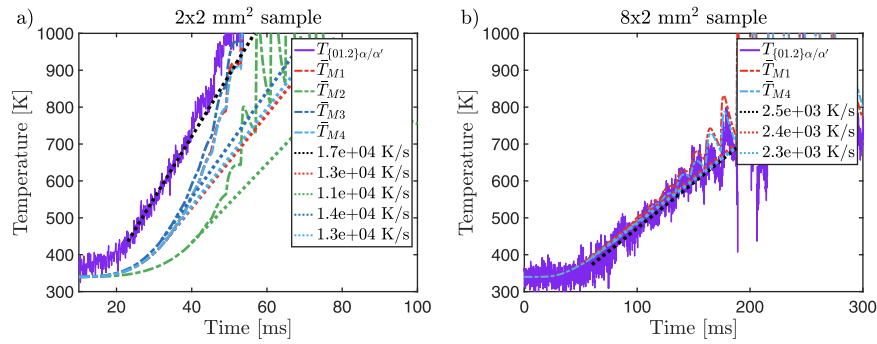
Fig. 15. Experimental and predicted temperature evolution in A$_X$ when the laser approaches (a) for the 2 × 2 mm sample, (b) for the 8 × 2 mm sample. For the 2 × 2 sample, the predicted heating rates are shown when temperature reached 440 K.
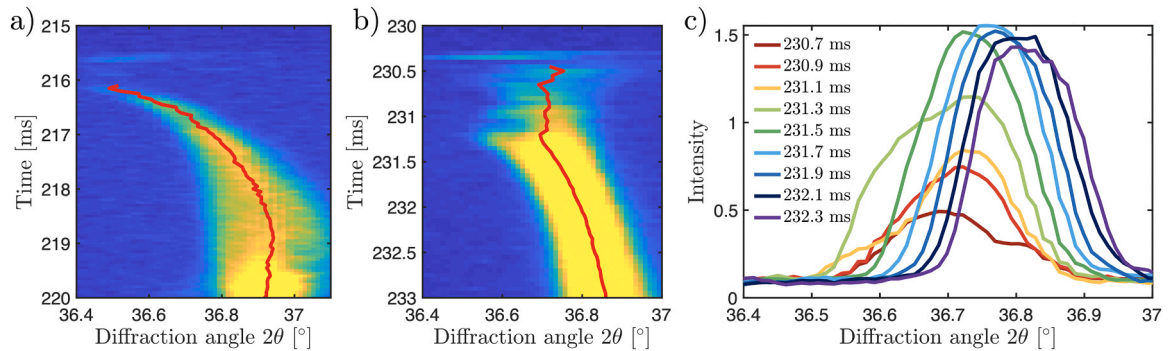

Fig. 16. Peak position evolution for the 8 × 2 mm^2 sample from temperature peaks 1 (a) and 2 (b) indicated on Fig. 12; (c) evolution of the peak intensity for (b) over time.

Fig. 12 b. The figures represent the intensity evolution of the β phase over time, with the peak position calculated using the center of mass indicated with a red line. For cycle 1 beginning at t ≈ 216 ms (Fig. 16a), the centre of mass describes nicely the peak position shift during cooling and, therefore, will give a good estimation of the temperature evolution in A$_X$. However, for cycle 2 starting around t = 230.5 ms (Fig. 16b) the situation is more complex. In the beginning after solidification (230.5 ms) the center of mass seems to be affected by intensity contributions of a β grain that is at a much lower temperature than expected. This is also visible in Fig. 16c showing individual diffraction patterns at selected time instants. At t = 231.5 ms, a second high-intensity contribution joins the diffraction pattern, after which the center of mass follows well the intensity of the resulting peak.

The complex evolution of the diffracted $\{002\}\beta$ intensity in cycle 2 can be explained by contributions of α/α' grains that are located in the heat-affected zone of the laser but not in the melt pool. Such a grain will transform into β upon heating, however not melt. Furthermore, β grains

formed during cooling down from the melt, might not contribute always to the diffracted intensity. For easier understanding, a schematics of the above situation is presented in Fig. S1 of the Supplementary Data.

The above-detailed analysis of the diffraction profiles in cycles 1 and 2 demonstrates that the calculation of the β cooling rates should be done while visually inspecting the evolution of the diffraction pattern. Using an average over the cycles closest to maximum overlap is recommended.

To obtain an average cooling rate, the three cycles around the maximum temperature in Fig. 11b and Fig. 12b have been taken into account in the simulated models and the experiment. The results are detailed in Figs. S2 and S3 of the Supplementary Data and summarized in Table 5 below.

The average experimental cooling rate of the β phase in the 2 × 2 mm^2 sample is -3.7×10^5 K/s. The cooling rates as well as the shape of the cooling curve are rather well predicted by model M3 and M4 as shown in Fig. 11b. These models include an larger laser penetration depth and enhanced thermal conductivity. The maximum temperature of the β phase predicted by M3 is close to the experimental value (1900 K) and is 100 K lower for M4. The predicted temperature before the laser comes back is 100 K lower in M3 compared to the experiment and 170 K lower in M4. These differences can be explained by the radiation loss that is taken into account in M4. Models M1 and M2 overestimate the cooling rate. M1 predicts a similar maximal β temperature as M3, whereas M2 predicts only a maximum value close to 1600 K.

The experimental cooling curve for the 8 × 2 mm^2 sample has two sections: the first represents the cooling of the β phase, the second the cooling of the α/α' phase (Fig. 12). As shown in [27], upon the transformation of parts of the X-ray probed surface region from β to α, the β phase exhibit residual stress. Therefore the last part of the experimental β cooling curve is not solely driven by thermal contraction. The predicted cooling curves lie in between the experimental α/α' and β cooling curve (Fig. 12b). The experimentally measured average cooling rate of

Table 5
Cooling rate in the β phase.

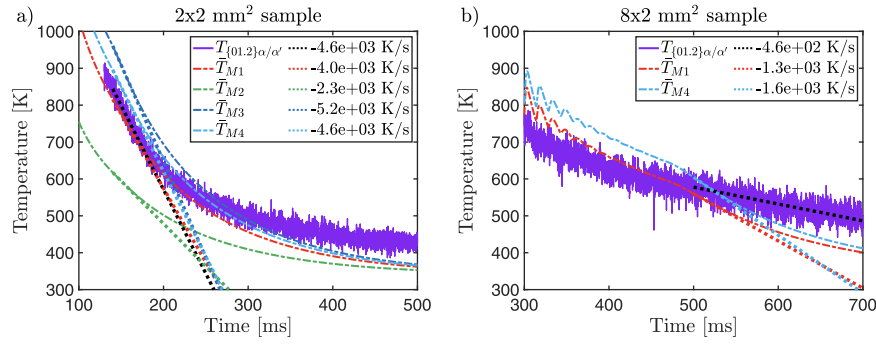|	Experimental	M1	M2	M3	M4
Cooling rates from 2 × 2 mm^2 sample ($10^5 K/s$)					
Cycle 1	− 2.3	− 4.7	− 5.2	− 2.6	− 2.5
Cycle 2	− 4.9	− 5.5	− 7.4	− 3.2	− 3.3
Cycle 3	− 3.8	− 4.2	− 4.5	− 2.6	− 2.4
Average	− 3.7	− 4.8	− 5.7	− 2.8	− 2.7
Cooling rates from 8 × 2 mm^2 sample ($10^5 K/s$)					
Cycle 1	− 4.6	− 6.2	N/A	N/A	− 2.7
Cycle 2	− 2.7	− 6.8	N/A	N/A	− 4.9
Cycle 3	− 5.1	− 5.0	N/A	N/A	− 2.8
Average	− 4.1	− 6.0	N/A	N/A	− 3.5

Fig. 17. Temperature evolution in the α/α' phase and cooling rates at the moment the laser is switched off: (a) the 2×2 mm^2, laser switched off at t $\approx$ 140 ms; (b) 8×2 mm sample, laser switched off at t $\approx$ 500 ms.

the β phase (-4.1×10^5 K/s) is of the same order of magnitude as the one measured in the 2×2 mm^2 sample. The trends predicted by M1 and M4 are similar as in the 2×2 mm^2 sample: M1 predicts a comparable maximum temperature but a too high cooling rate, the maximal temperature predicted by M4 is lower, but the average cooling rate are not so far from the experimental one. Both models slightly overestimate the temperature of the α/α' phase by around 100 K.

4.2.3. Cooling rates after laser scanning

Fig. 17 shows the cooling curves after the laser is scanning the last lines (therefore far away from A_X) and after the laser is switched off (a) for the 2×2 mm^2 and (b) the 8×2 mm^2 sample. In both samples, the X-ray probed volume remains in the α/α' phase. The cooling rates (shown by dotted curves, values given in caption) are calculated for the moment the laser is switched off. This is at t = 140 ms in the 2×2 mm^2 sample and t = 500 ms in the 8×2 mm^2 sample.

When the laser is switched off, the temperature of the α/α' phase predicted by M1 agrees well with the experimental measures for both types of samples. In the 2×2 mm^2 sample this temperature corresponds to 880 K, whereas it is 600 K in the 8×2 mm^2 sample. The model M3 predicts higher temperatures in the 2×2 mm^2 sample, adding the radiation loss (M4) reduces this temperature but the values are still higher than experimentally measured (also for the 8×2 mm^2 sample). The predicted temperature of M3 is 200 K below that of M1.

The experimental cooling rates at the moment the laser is switched off is a factor of 10 lower in the 8×2 mm^2 sample (-4.6×10^2 K/s) compared to the 2×2 m^2 sample (-4.6×10^3 K/s) because of the higher accumulated temperature and the fact that the heat losses are directly proportional to the temperature (Section 2.1.3). It is however interesting to look at the shape of the cooling curves predicted by M1 and M4 in both samples. When temperatures are still high (above $\approx$550 K) the predictions for 2×2 mm^2 sample (except M3) follow well the shape of the experimental curve, but once below 550 K the predicted values get much lower. Remarkably, the temperature predicted by all

models is very similar i.e. $\approx$340 K (the temperature of the substrate) whereas the experimental values suggest 100 K higher. A similar trend is observed in the 8×2 sample, where below 550 K, the computational samples cool down much faster than the experimental ones.

When comparing experimental and predicted cooling curves, one has however to keep in mind that the experimental temperature is derived assuming that the change in lattice parameter is solely due to thermal expansion/contraction. Measurements reveal however important anisotropy in the lattice strain among the different reflections (Fig. 18). In the above analysis, temperatures were derived considering the X-ray diffraction peak {01.2}α/α'. Compared to the initial lattice distance measured at 340 K, these lattice planes get into tension after cooling, whereas others get into compression such as, for instance, the {01.0}$\alpha\alpha/$ α' in the 8×2 mm^2 sample.

Fig. 18 shows the simulated and experimental temperature profile calculated from the different α/α' diffraction peaks (a) for the 2×2 mm^2 sample, (b) for the 8×2 mm^2 sample. Deriving the temperature from different reflections can give variations of up to 500 K in the large sample, less in the smaller sample. Deriving the correct values requires detailed knowledge of the elastic-plastic anisotropy as well as taking into account the difference in the texture of the samples [27].

In summary, the models M1 and M4 catch quite well the immediate cooling rates of the β phase after the laser has passed A_X as well as the shape of the cooling curves. The predicted values of maximum β temperature are good for M1 and M3, but adding radiation loss to M3 reduces these temperatures again. Differences in cooling behavior of the α/α' phase after the laser has traveled far away from the X-ray probed area or after the laser is switched off, suggests the importance of the introduction of elastic/plastic anisotropy in the models. To address the sluggish heating transfer to the α/α' phase in the 2×2 mm^2 (not present in the 8×2 mm^2 sample) we explore the influence of the mesh size and anisotropic enhanced thermal conductivity.
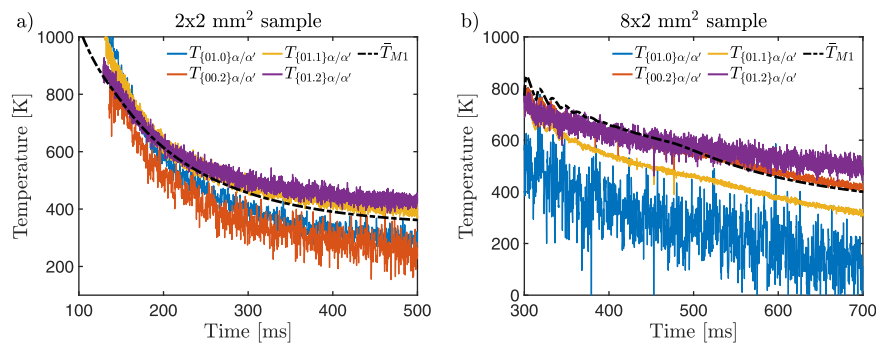

Fig. 18. Temperature profile in the α/α' phase calculated from the different reflections (Fig. 6) (a) for the 2×2 mm^2, (b) for the 8×2 mm^2 sample. For comparison, the temperatures predicted by model M1 are added.
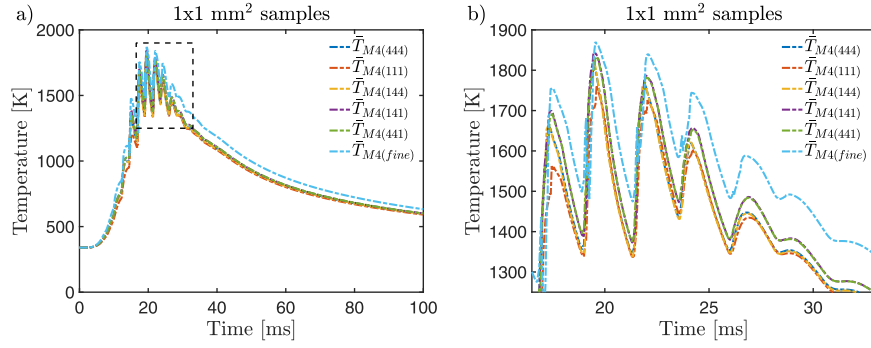
Fig. 19. Overall temperature profile for the different simulated models; (b) Detailed profiles zoomed in the highlighted area in (a) around the instant when the laser cross A_X (t ≈ 20 ms).

4.3. The role of enhanced thermal conductivity and mesh size

In M4 an isotropic thermal conductivity coefficient was used above the melting point (Eq. (14)) in order to mimic Marangoni effects. The value $\lambda = 4$ was chosen to obtain a melt pool shape that matches the width and depth of a single track [7]. Previously, it has been demonstrated that heat gradients could be modified by introducing an anisotropic enhancement coefficient, influencing the temperature profile within the sample [47].

To investigate the influence of anisotropic versus isotropic enhanced thermal conductivity, a 1×1 mm² sample was simulated using M4 with different values of the enhancement parameters in the three principal directions. The temperature profiles were extracted with the same X-ray beam weighted averaging technique. The overall temperature evolution is shown in Fig. 19a, details are provided in the zoom-in around the cycle

where the laser crosses A_X (Fig. 19b). The curves are labeled $\overline{T}_{M4(XYZ)}$; X, Y and Z being the value of the enhancement coefficient in the X, Y, and Z directions respectively. The curve labeled $\overline{T}_{M4(444)}$ corresponds to the reference sample with an isotropic coefficient of 4 as used in the original M4 simulation (Eq. (14)). Furthermore, to explore the role of mesh size, a 1×1 mm² sample was simulated with an isotropic enhancement coefficient of 4 and a finer meshing element size of 30×30×30 μm². The curve is labeled $\overline{T}_{M4(fine)}$.

Changing the enhancement parameter in all three directions ($\overline{T}_{M4(111)}$ vs $\overline{T}_{M4(444)}$) or only in the (Y,Z) directions ($\overline{T}_{M4(111)}$ vs $\overline{T}_{M4(144)}$) has little impact on the temperature profile in the high-temperature regime. Increasing the enhancement coefficient in the Y-direction ($\overline{T}_{M4(111)}$ vs $\overline{T}_{M4(141)}$), or the (X,Y) directions ($\overline{T}_{M4(111)}$ vs $\overline{T}_{M4(441)}$) slightly increases the temperature profile by about 40 K on average. Reducing
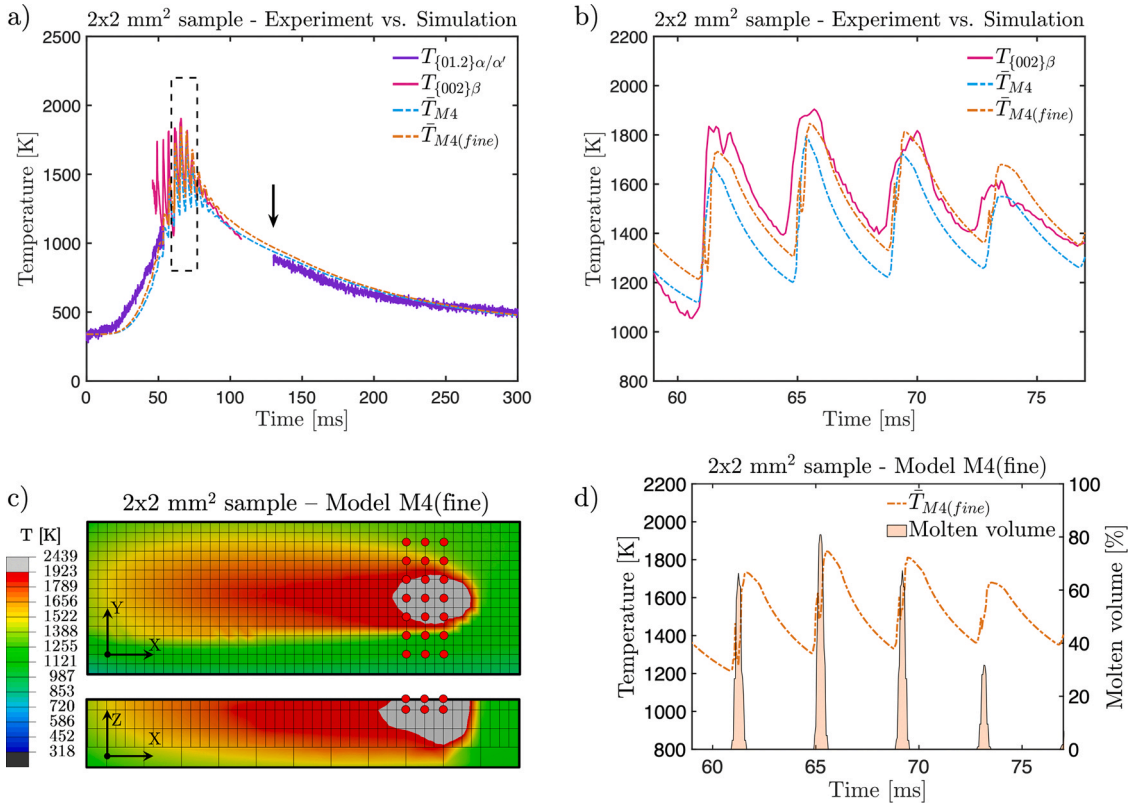

Fig. 20. (a) Experimental temperature evolution derived from the $(01.2)\alpha/\alpha'$ and $\{002\}\beta$ reflections in purple and pink, respectively, and simulated results for model M4 and M4(fine) in dashed lines; (b) Zoom on the highlighted area in (a); (c) Top view and cross-section of the simulated melt pools for model M4(fine) at t ≈ 65 ms, when the laser beam overlaps with A_X; (d) Average temperature and molten volume interaction with A_X for M4 (fine). (For interpretation of the references to colour in this figure legend, the reader is referred to the web version of this article.)

14

the mesh size has however a bigger influence on the temperature profile (curve $\overline{T}_{M4(fine)}$). This is evident when comparing $\overline{T}_{M4(444)}$ with $\overline{T}_{M4(fine)}$, where the mesh size in the (XY) plane was reduced from 60 μm to 30 μm. The temperature profile of the smaller meshed sample shifts up by about 100 K on average.

To verify the influence of the mesh size with our experimental data, a 2×2 mm^2 sample was simulated with the model M4 and the fine mesh – M4(fine). Fig. 20a compares the experimental data, pink for the β phase and purple for the α/α' phase. The predictions for model M4 are shown in light blue, for the model M4 with refined mesh in orange. The laser scanning starts at t = 0 ms, and the black arrow shows when the laser beam is switched off. The laser crosses A$_X$ at t ≈ 65 ms. Fig. 20c shows the predicted melt pool dimensions for M4(fine). Fig. 20d shows temperature evolution and the molten volume during 4 cycles evolution around t ≈ 65 ms. The refinement of the mesh in the (X,Y) plane improves the heat flow in these directions. As a result, the melt pool width and length increase (see Fig. 10h), the depth stays the same. The overall temperature profiles shift to higher values by 50 K and are now closer to the experimental data. During the initial heating, the simulated curve remains however lagging. In other words, refining the mesh diminishes the difference between experimental and predicted values because the heat can travel better to A$_X$. However, some differences remain pointing to the role of material parameters used in the simulations. The size of the melt pool has slightly increased in the width, now measuring around 150 μm, and in the length with 270 μm. The depth remains the same, at 150 μm.

5. Conclusion

Four FEM based models M1-M4 have been used to simulate printing of a 2×2 mm^2 and an 8×2 mm^2 Ti-6Al-4V samples using the same laser and scanning parameters as in previous *operando* X-ray diffraction experiments. By using an appropriate thermal expansion coefficient, *operando* XRD can resolve the local evolution of the temperature in real time. Compared to high-speed cameras, *operando* XRD provide simultaneously detailed information on the evolution of the phases during the printing of the last deposited layer. Furthermore, it has the potential to provide information on the phase dependent residual stresses after solidification. The temperature evolution, heating and cooling rates and melt pool dimensions have been compared with the experimentally obtained values. The following conclusions can be made:

- A simple ellipsoid laser heat source model (M1) predicts well the heating and cooling rates of the α/α' phase, as well as the melt pool length. The cooling rate of the β phase is too high, which might be related to the shallow depth of the melt pool.
- The double ellipsoid model (M2) has for the parameters used, shortcomings in the prediction of the temperatures reached in α/α' and β phase, the width, depth, and length of the melt pool are too small
- A cylindrical heat source with parabolic penetration depth and enhanced isotropic thermal conductivity (M3/M4) predicts a close to similar temperature evolution as M1, the cooling rate of the β phase is closer to the experimental value. When no radiation loss is incorporated, the maximum temperature of the β phase is well predicted, adding radiation loss brings the temperatures down. Cooling rates are not affected by radiation loss. The melt pool length and width are too small, the depth is comparable with experimental measurements.
- The simple ellipsoid model M1 is the only model that correctly predicts the melt pool length, it is characterized by the longest heat flux tail on the XY surface. Melt pool width and depth are however best described by the cylindrical heat source.
- Implementing anisotropy in the enhanced thermal conductivity does not affect the results for M3/M4

- Refining the mesh in M4 (at the cost of computer time) improves the prediction of the temperature evolution to a near-perfect match, it has however little or no effect on the heating and cooling rate of the α/α' phase.
- The influence of the small scan vector on the temperature evolution can be captured by both the simple ellipsoid laser heat source as well as the cylindrical source.

Our results show that *operando* X-ray SLM experiments can be used for validating temperature profiles predicted by FEM based models. Moreover, since such experiments provide direct measurements of lattice strains, the results can be used for further development of phase informed and thermomechanical inspired FEM based models.

CRediT authorship contribution statement

Samy Hocine: Conceptualization, Methodology, Software, Formal analysis, Investigation, Resources, Writing - original draft, Writing - review & editing, Visualization. **Helena Van Swygenhoven:** Conceptualization, Methodology, Investigation, Resources, Writing - original draft, Writing - review & editing, Supervision, Project administration, Funding acquisition. **Steven Van Petegem:** Methodology, Software, Formal analysis, Investigation.

Declaration of Competing Interest

The authors declare that they have no known competing financial interests or personal relationships that could have appeared to influence the work reported in this paper.

Acknowledgements

Appendix A. Supporting information

Supplementary data associated with this article can be found in the online version at doi:10.1016/j.addma.2020.101747.

References

[1] Z. Mao, D.Z. Zhang, P. Wei, K. Zhang, Manufacturing feasibility and forming properties of Cu-4Sn in selective laser melting, Materials 10 (2017) 333, https://doi.org/10.3390/ma10040333.

[2] J.J. Lewandowski, M. Seifi, Metal additive manufacturing: a review of mechanical properties, Annu. Rev. Mater. Res. 46 (2016) 151–186, https://doi.org/10.1146/annurev-matsci-070115-032024.

[3] D.K. Do, P. Li, The effect of laser energy input on the microstructure, physical and mechanical properties of Ti-6Al-4V alloys by selective laser melting, Virtual Phys. Prototyp. 11 (2016) 41–47, https://doi.org/10.1080/17452759.2016.1142215.

[4] S. Liu, Y.C. Shin, Additive manufacturing of Ti6Al4V alloy: a review, Mater. Des. 164 (2019), 107552, https://doi.org/10.1016/j.matdes.2018.107552.

[5] J.P. Oliveira, A.D. LaLonde, J. Ma, Processing parameters in laser powder bed fusion metal additive manufacturing, Mater. Des. 193 (2020), 108762, https://doi.org/10.1016/j.matdes.2020.108762.

[6] L.-X. Lu, N. Sridhar, Y.-W. Zhang, Phase field simulation of powder bed-based additive manufacturing, Acta Mater. 144 (2018) 801–809, https://doi.org/10.1016/j.actamat.2017.11.033.

[7] H. Ali, H. Ghadbeigi, K. Mumtaz, Residual stress development in selective laser-melted Ti6Al4V: a parametric thermal modelling approach, Int J. Adv. Manuf. Technol. 97 (2018) 2621–2633, https://doi.org/10.1007/s00170-018-2104-9.

[8] E. Mirkoohi, D.E. Seivers, H. Garmestani, S.Y. Liang, Heat source modeling in selective laser melting, Materials 12 (2019) 2052, https://doi.org/10.3390/ma12132052.

[9] H.-C. Tran, Y.-L. Lo, Heat transfer simulations of selective laser melting process based on volumetric heat source with powder size consideration, J. Mater. Process. Technol. 255 (2018) 411–425, https://doi.org/10.1016/j.jmatprotec.2017.12.024.

[10] J. Yang, S. Sun, M. Brandt, W. Yan, Experimental investigation and 3D finite element prediction of the heat affected zone during laser assisted machining of Ti6Al4V alloy, J. Mater. Process. Technol. 210 (2010) 2215–2222, https://doi.org/10.1016/j.jmatprotec.2010.08.007.

[11] V.D. Fachinotti, M. Bellet, Linear tetrahedral finite elements for thermal shock problems, Int. J. Numer. Methods Heat. Fluid Flow. 16 (2006) 590–601, https://doi.org/10.1108/09615530610669120.

[12] P. Tan, F. Shen, B. Li, K. Zhou, A thermo-metallurgical-mechanical model for selective laser melting of Ti6Al4V, Mater. Des. 168 (2019) 107642, https://doi.org/10.1016/j.matdes.2019.107642.

[13] Y. Zhang, G. Guillemot, M. Bernacki, M. Bellet, Macroscopic thermal finite element modeling of additive metal manufacturing by selective laser melting process, Comput. Methods Appl. Mech. Eng. 331 (2018) 514–535, https://doi.org/10.1016/j.cma.2017.12.003.

[14] K. Zeng, D. Pal, H.J. Gong, N. Patil, B. Stucker, Comparison of 3DSIM thermal modelling of selective laser melting using new dynamic meshing method to ANSYS, Mater. Sci. Technol. 31 (2015) 945–956, https://doi.org/10.1179/1743284714Y.0000000703.

[15] A. Olleak, Z. Xi, Simulation of layer-by-layer selective laser melting process with an efficient remeshing technique, Procedia Manuf. 34 (2019) 613–618, https://doi.org/10.1016/j.promfg.2019.06.167.

[16] Z. Luo, Y. Zhao, A survey of finite element analysis of temperature and thermal stress fields in powder bed fusion Additive Manufacturing, Addit. Manuf. 21 (2018) 318–332, https://doi.org/10.1016/j.addma.2018.03.022.

[17] K. Khan, A. De, Modelling of selective laser melting process with adaptive remeshing, Sci. Technol. Weld. Join. 24 (2019) 391–400, https://doi.org/10.1080/13621718.2019.1575057.

[18] H. Ghasemi-Tabasi, J. Jhabvala, E. Boillat, T. Ivas, R. Drissi-Daoudi, R.E. Logé, An effective rule for translating optimal selective laser melting processing parameters from one material to another, Addit. Manuf. 36 (2020) 101496, https://doi.org/10.1016/j.addma.2020.101496.

[19] Y. Du, X. You, F. Qiao, L. Guo, Z. Liu, A model for predicting the temperature field during selective laser melting, Results Phys. 12 (2019) 52–60, https://doi.org/10.1016/j.rinp.2018.11.031.

[20] B. Liu, B.-Q. Li, Z. Li, P. Bai, Y. Wang, Z. Kuai, Numerical investigation on heat transfer of multi-laser processing during selective laser melting of AlSi10Mg, Results Phys. 12 (2019) 454–459, https://doi.org/10.1016/j.rinp.2018.11.075.

[21] Q. Zhang, J. Xie, Z. Gao, T. London, D. Griffiths, V. Oancea, A metallurgical phase transformation framework applied to SLM additive manufacturing processes, Mater. Des. 166 (2019) 107618, https://doi.org/10.1016/j.matdes.2019.107618.

[22] H.-S. Tran, J.T. Tchuindjang, H. Paydas, A. Mertens, R.T. Jardin, L. Duchêne, R. Carrus, J. Lecomte-Beckers, A.M. Habraken, 3D thermal finite element analysis of laser cladding processed Ti-6Al-4V part with microstructural correlations, Mater. Des. 128 (2017) 130–142, https://doi.org/10.1016/j.matdes.2017.04.092.

[23] M. Chiumenti, E. Neiva, E. Salsi, M. Cervera, S. Badia, J. Moya, Z. Chen, C. Lee, C. Davies, Numerical modelling and experimental validation in Selective Laser Melting, Addit. Manuf. 18 (2017) 171–185, https://doi.org/10.1016/j.addma.2017.09.002.

[24] C. Bruna-Rosso, A.G. Demir, B. Previtali, Selective laser melting finite element modeling: validation with high-speed imaging and lack of fusion defects prediction, Mater. Des. 156 (2018) 143–153, https://doi.org/10.1016/j.matdes.2018.06.037.

[25] B. Gould, S. Wolff, N. Parab, C. Zhao, M.C. Lorenzo-Martin, K. Fezzaa, A. Greco, T. Sun, In situ analysis of laser powder bed fusion using simultaneous high-speed infrared and x-ray imaging, JOM (2020), https://doi.org/10.1007/s11837-020-04291-5.

[26] P.A. Hooper, Melt pool temperature and cooling rates in laser powder bed fusion, Addit. Manuf. 22 (2018) 548–559, https://doi.org/10.1016/j.addma.2018.05.032.

[27] S. Hocine, H. Van Swygenhoven, S. Van Petegem, C.S.T. Chang, T. Maimaitiyili, G. Tinti, D. Ferreira Sanchez, D. Grolimund, N. Casati, Operando X-ray diffraction during laser 3D printing, Mater. Today (2019), https://doi.org/10.1016/j.mattod.2019.10.001.

[28] S. Hocine, S. Van Petegem, U. Frommherz, G. Tinti, N. Casati, D. Grolimund, H. Van, A miniaturized selective laser melting device for operando X-ray

[29] diffraction studies, Addit. Manuf. 34 (2020), 101194, https://doi.org/10.1016/j.addma.2020.101194.

[29] Abaqus Unified FEA - SIMULIATM by Dassault Systèmes®, (n.d.). https://www.3ds.com/products-services/simulia/products/abaqus/. (Accessed 25 March 2020).

[30] K.C. Mills, Recommended values of thermophysical properties for selected commercial alloys, Woodhead, Cambridge, 2002.

[31] D.A. De Moraes, A. Czekanski, Parametric thermal FE analysis on the laser power input and powder effective thermal conductivity during selective laser melting of SS304L, J. Manuf. Mater. Process. 2 (2018) 47, https://doi.org/10.3390/jmmp2030047.

[32] U. Ali, Y. Mahmoodkhani, S. Imani Shahabad, R. Esmaeilizadeh, F. Liravi, E. Sheydaeian, K.Y. Huang, E. Marzbanrad, M. Vlasea, E. Toyserkani, On the measurement of relative powder-bed compaction density in powder-bed additive manufacturing processes, Mater. Des. 155 (2018) 495–501, https://doi.org/10.1016/j.matdes.2018.06.030.

[33] S.S. SIH, J.W. BARLOW, The prediction of the emissivity and thermal conductivity of powder beds, Part. Sci. Technol. 22 (2004) 427–440, https://doi.org/10.1080/02726350490501682.

[34] T. Hoshino, K. Mito, A. Nagashima, M. Miyata, Determination of the thermal conductivity of argon and nitrogen over a wide temperature range through data evaluation and shock-tube experiments, Int J. Thermophys. 7 (1986) 647–662, https://doi.org/10.1007/BF00502397.

[35] A.V. Gusarov, E.P. Kovalev, Model of thermal conductivity in powder beds, Phys. Rev. B 80 (2009), 024202, https://doi.org/10.1103/PhysRevB.80.024202.

[36] H. Ali, Evolution of Residual Stress in Ti6Al4V Components Fabricated Using Selective Laser Melting, (Ph.D. thesis), University of Sheffield, 2017 (Accessed 3 February 2020), http://etheses.whiterose.ac.uk/18039/.

[37] SIMULIATM Support Documentation - Dassault Systèmes®, (n.d.). https://www.3ds.com/products-services/simulia/services-support/support/documentation/. (Accessed 19 February 2020).

[38] A.K. Mishra, A. Aggarwal, A. Kumar, N. Sinha, Identification of a suitable volumetric heat source for modelling of selective laser melting of Ti6Al4V powder using numerical and experimental validation approach, Int. J. Adv. Manuf. Technol. 99 (2018) 2257–2270, https://doi.org/10.1007/s00170-018-2631-4.

[39] J. Goldak, A. Chakravarti, M. Bibby, A new finite element model for welding heat sources, MTB 15 (1984) 299–305, https://doi.org/10.1007/BF02667333.

[40] G. Tinti, A. Bergamaschi, S. Cartier, R. Dinapoli, D. Greiffenberg, I. Johnson, J. H. Jungmann-Smith, D. Mezza, A. Mozzanica, B. Schmitt, X. Shi, Performance of the EIGER single photon counting detector, C03011, J. Instrum. 10 (2015) C03011, https://doi.org/10.1088/1748-0221/10/C03011.

[41] T. Ahmed, H.J. Rack, Phase transformations during cooling in α+β titanium alloys, Mater. Sci. Eng.: A 243 (1998) 206–211, https://doi.org/10.1016/S0921-5093(97)00802-2.

[42] X. Tan, Y. Kok, W.Q. Toh, Y.J. Tan, M. Descoins, D. Mangelinck, S.B. Tor, K. F. Leong, C.K. Chua, Revealing martensitic transformation and α/β interface evolution in electron beam melting three-dimensional-printed Ti-6Al-4V, Sci. Rep. 6 (2016), https://doi.org/10.1038/srep26039.

[43] H. Shipley, D. McDonnell, M. Culleton, R. Coull, R. Lupoi, G. O'Donnell, D. Trimble, Optimisation of process parameters to address fundamental challenges during selective laser melting of Ti-6Al-4V: A review, Int. J. Mach. Tools Manuf. 128 (2018) 1–20, https://doi.org/10.1016/j.ijmachtools.2018.01.003.

[44] Y.S. Touloukian, R.K. Kirby, R.E. Taylor, P.D. Desai, Thermal Expansion, Springer,, US, Boston, MA, 1975, https://doi.org/10.1007/978-1-4757-1622-1.

[45] J.J.Z. Li, W.L. Johnson, W.-K. Rhim, Thermal expansion of liquid Ti–6Al–4V measured by electrostatic levitation, Appl. Phys. Lett. 89 (2006) 111913, https://doi.org/10.1063/1.2349840.

[46] H. Gong, H. Gu, K. Zeng, J. j. s Dilip, D. Pal, B. Stucker, D. Christiansen, J. Beuth, J. Lewandowski, Melt Pool Characterization for Selective Laser Melting of Ti-6Al-4V Pre-alloyed Powder, 2014.

[47] S. Safdar, A.J. Pinkerton, L. Li, M.A. Sheikh, P.J. Withers, An anisotropic enhanced thermal conductivity approach for modelling laser melt pools for Ni-base super alloys, Appl. Math. Model. 37 (2013) 1187–1195, https://doi.org/10.1016/j.apm.2012.03.028.